# Lotus seedpod-inspired internal vascularized 3D printed scaffold for bone tissue repair

Xiaoyu Han [a,b,1], Mingjie Sun [a,1], Bo Chen [b], Qimanguli Saiding [b], Junyue Zhang [a], Hongliang Song [a], Lianfu Deng [b], Peng Wang [a,**], Weiming Gong [a,***], Wenguo Cui [b,*]

[a] *Department of Orthopedics, Jinan Central Hospital, Shandong First Medical University & Shandong Academy of Medical Sciences, 105 Jiefang Road, Lixia District, Jinan, Shandong, 250013, PR China*
[b] *Shanghai Key Laboratory for Prevention and Treatment of Bone and Joint Diseases, Shanghai Institute of Traumatology and Orthopedics, Ruijin Hospital, Shanghai Jiao Tong University School of Medicine, 197 Ruijin 2nd Road, Shanghai, 200025, PR China*

## ARTICLE INFO

## ABSTRACT

In the field of bone defect repair, 3D printed scaffolds have the characteristics of personalized customization and accurate internal structure. However, how to construct a well-structured vascular network quickly and effectively inside the scaffold is essential for bone repair after transplantation. Herein, inspired by the unique biological structure of "lotus seedpod", hydrogel microspheres encapsulating deferoxamine (DFO) liposomes were prepared through microfluidic technology as "lotus seeds", and skillfully combined with a three-dimensional (3D) printed bioceramic scaffold with biomimetic "lotus" biological structure which can internally grow blood vessels. In this composite scaffold system, DFO was effectively released by 36% in the first 6 h, which was conducive to promote the growth of blood vessels inside the scaffold quickly. In the following 7 days, the release rate of DFO reached 69%, which was fundamental in the formation of blood vessels inside the scaffold as well as osteogenic differentiation of bone mesenchymal stem cells (BMSCs). It was confirmed that the composite scaffold could significantly promote the human umbilical vein endothelial cells (HUVECs) to form the vascular morphology within 6 h *in vitro*. *In vivo*, the composite scaffold increased the expression of vascularization and osteogenic related proteins Hif1-α, CD31, OPN, and OCN in the rat femoral defect model, significantly cutting down the time of bone repair. To sum up, this "lotus seedpod" inspired porous bioceramic 3D printed scaffold with internal vascularization functionality has broad application prospects in the future.

## 1. .Introduction

The physiological process of bone repair includes tissue development, maturation, and remodeling [1,2]. Osteogenesis and angiogenesis are two critical factors in the reconstruction of the stable and mature bone, in which the development of internal blood vessels is essential for the success of tissue engineering and bone regeneration. Because it can not only effectively transport the nutrients and metabolic waste needed by bone cells, but also maintain the internal homeostasis of bone tissue, and promote the (bone mesenchymal stem cells) BMSCs differentiate to osteoblasts, thus promising the success of bone regeneration [2,3]. Bioceramics have been recognized as excellent bone graft materials

because of their human bone-like Ca/P ratio and good biocompatibility as well as mechanical properties [4]. Through solid-phase, hydrothermal, and precipitation reactions, various types of porous bioceramics can be constructed to simulate the calcium phosphate structure of bone tissue [5,6]. However, as for precise design, it has not been fully controllable yet. In recent decades, the computer-aided 3D printing technology not only can correctly solve the processing problems of different bone defect models, but also accurately control the overall characteristics of the materials, and precisely simulate the pore size and porosity of cancellous bone, which has been identified as an effective way to construct a biomimetic tissue engineering scaffold [7–9]. The porous bioceramic scaffolds prepared by 3D printing technology possess

---

the biomimetic structures and the biomineralization abilities to induce bone regeneration, but it cannot achieve the internal vascularization effectively. For example, as new bone tissue usually grows in margin-to-center direction, the internal bone formation of the scaffold is low. Therefore, the construction of a bioceramic 3D printed scaffold that integrates internal growth of blood vessels, osteo-inductive activity, and the function of recruiting bone marrow mesenchymal stem cells is currently a significant challenge.

The healing process of bone tissue begins with inflammation following immune cells, releasing inflammatory factors at the initial stage, consequently recruiting BMSCs and guiding their osteogenic differentiation [10]. This process is also closely related to neovascularization [2]. At present, the most commonly used approach is integrating cytokines such as bone morphogenetic protein- 2 (BMP-2) [11] or vascular endothelial growth factor (VEGF) [8] to the scaffold for vascularization and recruitment of BMSCs. However, the preparation of bioceramic 3D printed scaffolds requires high-temperature sintering, which can quickly inactivate cytokines or drugs modified on the surface of the scaffold; on the other hand, the cytokines attached to the surface of the scaffold have a short half-life and low bio-activity *in vivo*; besides, the release rate of the drugs is too fast making it a challenge to vascularize inside the scaffold. Therefore, it is of great importance to find a drug with dual functions of vascularization and osteogenesis for bone repair. Recent studies have shown that hypoxia mimic complex deferoxamine (DFO) can activate the hypoxia-inducible factor 1-α pathway (Hif1-α), which can promote angiogenesis and differentiation of BMSCs into the osteoblasts while inhibiting the osteoclast precursor cells from differentiating into osteoclasts [12–15]. The combination of DFO and the bioceramic 3D printed scaffold makes it a functional scaffold with dual effects which are essential for bone defect regeneration. However, as a small water-soluble molecule, direct injection of DFO leads to easy deactivation and rapid degradation making it urgent to design a new drug delivery system to effectively combine DFO and bioceramic 3D printed scaffolds for the rapid repair of bone defects. Hydrogel microspheres were made via microfluidic technology for it has a special three-dimensional grid-like and a porous structure after freeze-drying making it a promising drug carrier for the past years [16]. The unique structure is not only facilitating the sustained release of target drugs *in vivo* but guaranteed the ideal drug release effects. However, due to its water-solubility, the sustained release effect is minimal when DFO is directly combined with hydrogels manifested as the quick loss of active molecules, causing excessive local drug concentration, which may lead to histotoxicity.

Given that, it is necessary to find a solution for the sustained release of DFO within hydrogels. Liposomes have a phospholipid bilayer structure in resemblance with cell membranes capable of delivering
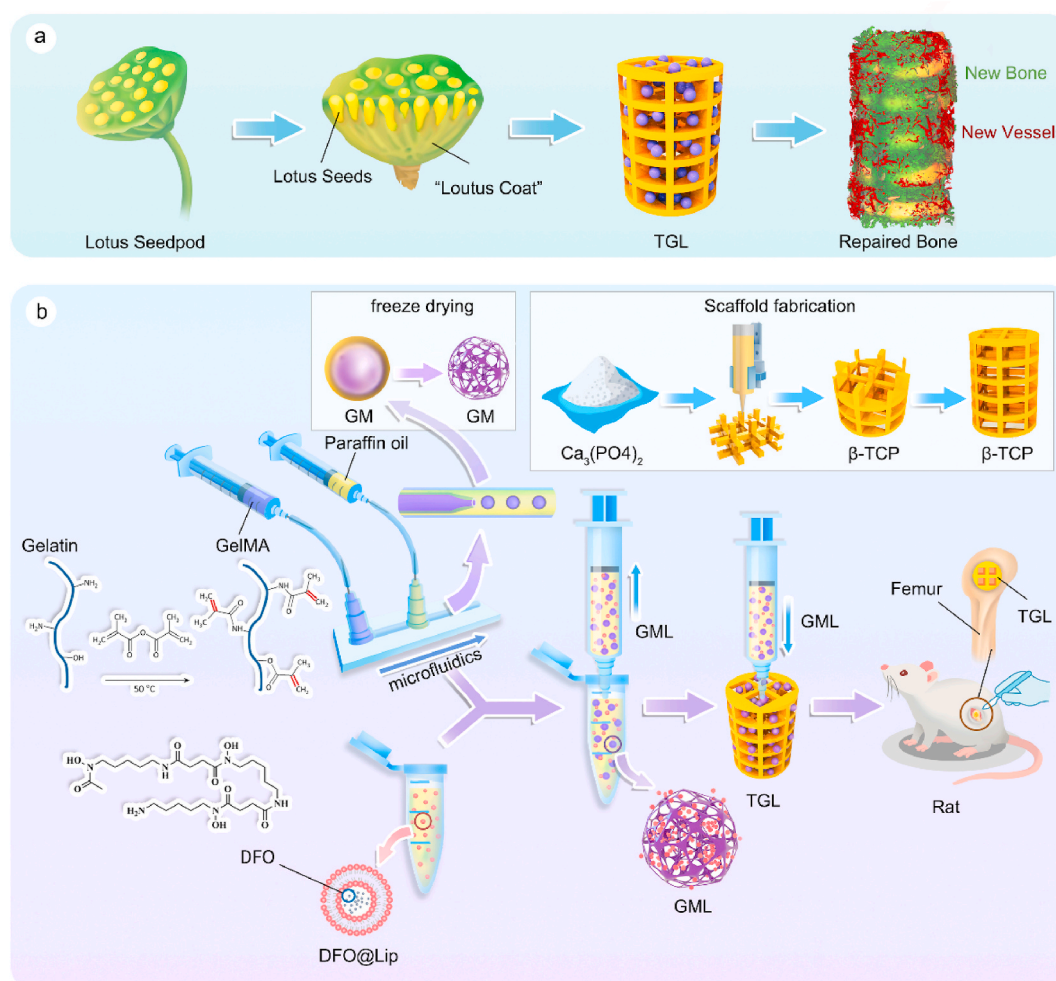


**Scheme 1. Schematic diagram of composite scaffold that incorporated GelMA microsphere @ Liposome (GML) into β - TCP scaffold (TGL) and its biological affects in bone repair process in rat bone defect model. (a)** The unique biological structure of lotus seedpod and inspirational. **(b)** Construction process of TGL scaffolds. The synthesized GelMA were made into microspheres (GM) using microfluidics and the DFO loaded liposomes were assembled into the microspheres (GML) via physical adsorption. Finally, the GML was integrated to β-TCP through direct injection to construct the composite TGL. The bone repair capabilities of composite scaffolds were studied in rat distant femur defect model.

both water and lipid soluble substances *in vivo* [17,18]. In this way, DFO-loaded liposomes are integrated into hydrogel microspheres by dipping and adsorbing, which effectively maintained the biological activity of DFO with an ideal controlled release rate better controlling the local drug concentration to avoid unnecessary side effects.

"Lotus seedpod" is a spongy receptacle that buries the pistil of the lotus flower, filled with honeycomb holes on the surface which gradually expands after fertilization and is called "lotus" and there is a small nut, the "lotus seed" in each hole [19,20]. Inspired by this unique biological structure and with the internal vascularization concept in mind, a 3D printed porous bioceramic scaffold was constructed that takes the role of the lotus "coat" while the DFO-liposome loaded injectable composite hydrogel microspheres as "lotus seeds". The "lotus seeds" are injected directly into the 3D printed scaffold to construct an internally vascularized "lotus" bioceramic 3D printed scaffold (TGL) to promote the repair bone defects (Scheme 1). The 3D printed scaffold provides mechanical support, considerable porosity, and the appropriate Ca/P ratio required for bone regeneration [7]. The hydrogel microspheres inside the scaffold can control the release of DFO to achieve the purpose of vascularization and stable osteogenesis [21]. The cell biocompatibility, cell proliferation, controlled release of DFO, vascularization, and osteogenesis of the composite scaffolds were investigated *in vitro. In vivo,* a rat distal femur defect model was constructed and evaluated the vascularization and bone formation function of the composite scaffold through Micro-CT and pathological section staining.

## 2. .Materials and methods

### 2.1. Preparation of 3D printed scaffold

β-TCP powder ($M_W = 310.18$, Sigma Aldrich, USA), photosensitive resin (WANHAO) were used for preparing 3D printed bioceramic scaffolds. The photo initiator diphenyl(2,4,6-trimethylbenzoyl)phosphine oxide (TPO) and dispersant (DCA-1228) were mixed to obtain a precursor. Scaffolds that were conforming to cancellous bone pores were predesigned by Autodesk to obtain stereolithography (STL) files. The obtained precursor was next polymerized and crosslinked by a DLP-based 3D printer (AUTOCERA-M, Beijing, China) following STL files. Each piece with a thickness of 50 μm was exposed for 3 s. On printing finished, 405 nm light source was used, and the printed scaffolds were separated from the prototype platform. After being washed with ethanol for 30 s, the unsolidified resin was removed. Then pure bioceramic scaffolds were obtained by sintering under 1350 °C with a heating rate of 2 °C/min for 3 h [22].

### 2.2. Preparation of GelMA

20 g gelatin was dissolved in 200 mL PBS for 3 h; then the swollen gelatin was stirred in a 60 °C water bath until the gelatin is completely dissolved under dark condition; 16 mL of methacrylic anhydride (MA) was slowly added using a microinjection pump at a speed of 0.25 mL/min and allowed to react for 2 h. The reaction was terminated with the addition of 800 mL of PBS. Next, GelMA solution was put into dialysis bags and stirred in deionized water before freeze-drying to obtain lyophilized GelMA.

### 2.3. Preparation of DFO liposomes

The reverse evaporation heating method was used to prepare DFO liposomes. Briefly, lecithin and cholesterol were dissolved in anhydrous ether with a ratio of 4:1 before transferring to a beaker, followed by the addition of DFO aqueous solution drop by drop, and a stable emulsion was obtained via ultrasonication. The organic solution was removed by vacuum evaporation in a 10 °C water bath to obtain colloidal products. The gelatin product was hydrated with deionized water before treating with ultrasound for 5 min; 0.45 μm and 0.22 μm microporous

membranes were used then to filter to obtain deferoxamine liposome solution. The unencapsulated drugs are separated by ultra-filtered centrifugation, and the encapsulation efficiency of DFO-Lip was detected by high performance liquid chromatography (HPLC, Waters, H-Class, US). 1 mL of DFO lip was placed on the upper layer of the ultra-filtration centrifuge tube ($M_W = 3000$), and centrifuged for 5 min at 5000 rpm. Once finished, 1 mL deionized water was added, and centrifuged again for 5 min at 5000 rpm and repeated three times. Also, for the release of DFO-Lip alone, 5 mL DFO-Lip solution was loaded into a dialysis bag ($M_W = 3500$), fastened with cotton thread, then immersed in 35 mL PBS and the release profile was investigated *in vitro* in a constant temperature shaker at 37 °C. Samples were collected at specific time points. The liquid in the lower layer was detected by HPLC with the following conditions: for mobile phase, tetrahydrofuran: phosphate buffer solution (70:930), under a flow rate of 1 mL/min, detection wavelength 220 nm, column temperature 30 °C, C18 chromatography: 150 mm × 4.6 mm × 5 μm.

### 2.4. Preparation of composite hydrogel microspheres and assembly of scaffold

The composite hydrogel was prepared by a self-made microfluidic device [23]. Briefly, 500 mg lyophilized GelMA was dissolved in 10 mL of deionized water. Once it is fully dissolved, 50 mg 2-hydroxy-4'-(2-hydroxyethyl) Oxy)-2-methylpropiophenon was added to prepare the aqueous phase; Also, 1.5 g span 80 (sorbitol monooleate) was dissolved in 30 g paraffin oil, and the oil phase was prepared. The hydrogel microspheres prepared by microfluidics were crosslinked by a blue light on the circulating refrigerating pump and washed with acetone and deionized water for three times after the cross-linking is finished (Fig. S1). The prepared microspheres were freeze-dried, and 2 mg of which was weighed and dissolved in the DFO as mentioned above aqueous solution. DFO liposomes were adsorbed onto the GelMA microspheres through immersion adsorption activity to form hydrogel microspheres @ DFO liposomes (GML), and then extracted with a syringe and injected directly into the scaffold. In this way, the two are physically combined to form Liposome @ GelMA @ β -TCP integrated scaffold (TGL).

### 2.4.1. Characterization of the scaffold

The original and assembled scaffolds were photographed by a digital camera, and the porosity of the 3D printed scaffold was measured by the liquid displacement method [24,25]. A dynamic light scattering device (DLS, Zetasizer, Malvern, Nano-ZS90) was used to analyze liposome particle size distribution. The surface morphology of the hydrogel microspheres prepared by microfluidics was observed by scanning electron microscopy (SEM, Hitachi SU5000) and the porosity data were analyzed by Image J software. At the same time, the composite GelMA hydrogel microspheres were added with fluorescent molecules containing liposomes and DFO, and the microstructures were observed by a fluorescence microscope. The compression measurement of printing axis (Z axis) was carried out under environmental conditions, using a universal testing machine (Instron- 5569), and the displacement was controlled by a rate of 10 mm/min. Three samples were measured for each group. The encapsulation efficiency was evaluated as the ratio between the total content of drug in liposome and the initial content of drug during the initial formulation (w/w).

$$EE(\%) = \frac{Total \quad content \quad of \quad drug \quad in \quad liposome}{Initial \quad content \quad of \quad drug \quad in \quad the \quad formulation} \times 100$$

The drug loading rate and the amount of released DFO were determined by HPLC. In short, the assembled scaffolds are packed in a dialysis bag with 3500 molecular weight, sealed with cotton thread at both ends, immersed in 37 °C 50 mL deionized water, and then shook in a 100 rpm/min constant temperature shaker until the maximum drug release is achieved. At the predetermined time points, 1 mL sample was taken

from the release medium, and 1 mL deionized water was added to it. The sample was tested by HPLC under the same HPLC conditions as before.

### 2.4.2. Biocompatibility of the scaffold

Rat MC3T3-E1 cells were chosen to investigate the biocompatibility of the scaffold. The MC3T3-E1 cells were co-cultured with the composite scaffold in a 24-well tissue culture plate at a density of $1 \times 10^4$/well, and cultured at 37 °C in a humidified incubator under 5% $CO_2$ in α-MEM supplemented with 10% fetal bovine serum, 100 mg/mL streptomycin, 100 U/mL penicillin (Life Technology). The cytotoxicity was analyzed by the CCK-8 reagent (ck04, Dojindo, Japan). Specifically, on day 1, 4, and 7, 0.5 mL of 10% CCK-8 reagent (DMEM: CCK-8 90:10) was added to each well. Incubated for 2 h, 100 μL of the incubation supernatant was extracted to measure the OD value with a microplate reader under a wavelength of 450 nm. Besides, a Live/Dead cell kit (Invitrogen, L3224, US) was used to further study the cell viability on the scaffolds. The cells on the scaffolds after incubation of 1,4 and 7 days were stained with 500 μL of combined dye for 20 min and then observed under a fluorescence microscope. Besides, at the same time points, the cells were washed three times with PBS and fixed with 4% paraformaldehyde for 20 min, treated with 0.1% (v/v) Triton X-100 for 15 min and washed again with PBS followed by staining with 0.2 mL of 5 μg/mL Alexa Fluor 594 phalloidin and 0.2 mL of 10 μg/mL 4, 6-diamino-2-benzoindole dilactate (DAPI) to label actin and nuclei respectively. Lastly, the labeled cells were detected through a laser scanning confocal microscope (LSCM, LSM800, ZEISS, Germany).

### 2.4.3. Tube formation investigation of scaffolds

Matrigel-coated confocal 24-well plates were used for angiogenesis experiments. After incubated with fresh DMEM for 1 h at 37 °C, HUVECs were cultured in each well with a density of $3 \times 10^4$/well followed by pacing the scaffold in a Transwell upper compartment cup with a diameter of 0.4 μm. Similarly, cells were fixed with 4% paraformaldehyde after 3 h and 6 h of incubation in a 37 °C humidified incubator under 5% $CO_2$, and the cell cytoskeleton and nucleus were stained in the same way mentioned above. Tube formation was observed with LSCM, and Image J software was used to further analysis including the total tube length, junction number, mesh number, and mesh in each group area (Area of meshes). The study was repeated in triplicate.

### 2.4.4. RT-qPCR

The expression of osteogenesis and angiogenesis-related genes including ALP, Runx2, Osterix, OCN, OPN, Hif1-α, and VEGF were detected through Real-time quantitative PCR (RT-qPCR), and Gapdh was used as a reference gene. Briefly, the sterilized composite scaffolds were placed in a 6-well plate and immersed in a complete medium for 1 h. BMSCs were cultured on the scaffolds with a density of $10^5$/ well . After 24 h of incubation with normal α-MEM, the medium was replaced by osteogenic induction medium (50 μg/mL ascorbic acid, 10 mM b-glycerophosphate, and $10^{-8}$ M dexamethasone). On days 7 and 14, gene analysis was carried out on the cells. In a nutshell, the cells were digested with trypsin, and the total RNA was extracted using Trizol reagent (Invitrogen, US). Immediately, cDNA was synthesized from the extracted mRNA through reverse transcription reaction using Prime Script RT reagent Kit (Takara, Japan). Next, Next, RT-PCR was conducted using an SYBR Green RT-PCR kit (Takara, Japan) and ABI Step One Plus Real-Time PCR System (Applied Biosystems, US). The samples were repeated three times, and all the above experiments were performed under the manufacturer's instructions. The primer sequences of each gene were shown in Supplementary Table 1. For the detection of angiogenic genes Hif1-α and VEGF, HUVECs were cultured in a 6-well cell culture plate with a cell density of $10^5$/well. 24 h later, the same gene analysis performance was carried out in a similar manner mentioned above.

### 2.4.5. Immunofluorescence staining

The relevant immunostaining was carried in the way described in previous studies [26,27]. Rat BMSCs were cultured in a 24-well plate with regular or osteo-inductive medium with the presence of the scaffolds throughout the cell culture process. At specific time points, the cells were fixed with 4% paraformaldehyde solution, washed with PBS, then 0.1% (v/v) Triton X-100 was applied to permeabilize for 15 min at room temperature. Being rinsed with PBS, the primary target antibodies Osterix (OSX, ab22552, 1:200), Collagen type 1 (Col1,ab34710,Abcam, 1:500), osteopontin (OPN,ab8448, Abcam, 1:1000) and osteocalcin (OCN,ab13420, Abcam, 1:100) were added and incubated at 4 °C overnight. A fluorescent-labeled secondary antibody was applicated at 37 °C for 1 h, a 1:500 diluted DAPI solution was applied to cover the nucleus. Cells were thoroughly washed with PBS three times and analyzed under LSCM. All studies were carried in triplicate.

### 2.4.6. Alkaline phosphatase staining

Being placed in the upper chamber of the Transwell, $3 \times 10^4$/well density of BMSCs were seeded onto the scaffolds in a 12-well plate. Simultaneously, the cells were seeded on the surface of the sterilized scaffolds directly with the same cell density. Similarly, the osteogenic induction medium was applied to the cells after 24 h of culture. After cultivation of 1, 4, and 7 days, the cells were stained with alkaline phosphatase (ALP Beyotime, P0321) kit, and the OD value was evaluated using a microplate reader at 405 nm. The experiment was carried out in triplicates.

### 2.4.7. Alizarin Red S activity

Alizarin red activity was conducted to show the mineralized nodules of BMSCs cultured with the scaffolds. Cell culturing procedure was the same as the ALP staining, and after 14 days of cell culture, cells were stained with Alizarin Red kit. 10% of acetic acid was added to the culture plates and incubated overnight to quantify the Alizarin Red staining. After centrifuging for 15 min, the supernatant was extracted and mixed with 10% ammonium hydroxide. Next, 100 μL supernatant was extracted, and the OD value was read in the same way mentioned above. The samples were repeated in triplicates.

### 2.4.8. Western-blot

BCA protein assay kit was used to extract total cellular protein. Next, sample proteins were subjected to SDS electrophoresis followed by transferring onto a PVDF membrane (0.45 μm, Millipore, USA). 5% BSA used to block unspecific binding for 1 h, the membranes were incubated at 4 °C overnight with related primary antibodies including Hif1-α (ab1, Abcam, 1:200), VEGF (NB100-664, Novus, 1:1000). Washed three times with TBS, an HRP-conjugated secondary antibody (1:10,000) was applicated onto the membranes. After detected by an enhanced chemiluminescence system, antigen-antibody complexes were further quantified through using Image J software.

### 2.4.9. Bone repair assessment in vivo

Rat distal femoral bone defect model was established for in vivo bone repair assessment: 8-week-old male Sprague Dawley (SD) rats (Shanghai SLAC Laboratory, China) were bought, and after two weeks of adaptation, the animals (300 ± 50g) were anesthetized with 2.5% sodium pentobarbital (40 mg/kg), the lateral longitudinal incision of the distal femur is taken to expose the lateral femoral condyle, the center of the lateral femoral condyle was drilled with a 2.6 mm electric drill until it penetrates double cortex (Fig. S3). The prepared scaffold is implanted into the bone defect site, and the surgical incision is sutured successfully. A total of 30 rats were divided into three groups making n = 10 for control, β-TCP, and TGL groups, respectively.

### 2.4.10. Radiographic evaluation

The target animals were sacrificed at week 2 and week 4 for evaluating the bone repairing effects of the scaffolds. The femurs where the

scaffolds put in were harvested and fixed with 4% paraformaldehyde solution followed by an immediate performance of Micro CT scanning and 3D reconstruction of the bone defect area. The bone tissue volume/total tissue volume (BV/TV), bone mineral density (BMD), trabecular separation/spacing (Tb.Sp) as well as trabecular thickness (Tb·Th) were obtained for further analysis. All the above tests were repeated with three samples.

### 2.4.11. Histological tests and immunohistochemical analysis

After fixation with 4% paraformaldehyde for seven days, the tissue samples and then the tissue fixation fluid was changed twice. Then the samples were placed in 10% ethylene diamine tetraacetic acid (EDTA) for decalcification before embedded in paraffin, and 5 μm thick sections were stained with hematoxylin and eosin (HE). For the immunostaining process, the samples were air-dried, permeabilized with 0.1% Triton X-100 for 20 min, followed by a blockage in 5% BSA at room temperature for 20 min before incubated in primary antibodies such as Hif1-α (ab1, Abcam, 1:200), CD31 (NB100-2284, Novus, 1:2000), osteopontin (OPN, ab8448, Abcam, 1:1000) and osteocalcin (OCN, ab13420, Abcam, 1:100) at 4 °C overnight. Washed with PBS, a suitable Alexa fluorescent-conjugated secondary antibody (Molecular Probes, 1:4000, Life Tech,

USA) was applicated for 1 h at room temperature. After nuclei were counterstained with DAPI, and the sections were analyzed under LSCM. Similarly, Image J software was used to quantify the immunological signal intensity. All specimens were repeated with five sections.

### 2.4.12. Hard tissue section

For the double fluorescent labeling of Alizarin Red and Calcein, the rats were subjected to subcutaneous injection within the bone defect area of Alizarin Red (3 mg/100g) and Calcein (2 mg/100g) 10 days and three days before euthanasia after 2 and 4 weeks after surgery respectively [28]. Rats were sacrifice at given time points, and the explants were fixated in 70% ethanol at 4 °C for two days. Acetone was used to dehydrate following embedment in methyl methacrylate. A microtome (Leica, RM2255, Germany) was used to cut 10-μm femoral slices and was displayed with a laser microscope (LSCM). We also used Image J software to calculate the mineral coordination rate (MAR). All experiments were repeated with 5 specimens.

### 2.4.13. Data statistics and processing

In this study, each experimental section was repeated three times, and the result of each study was expressed as mean ± standard
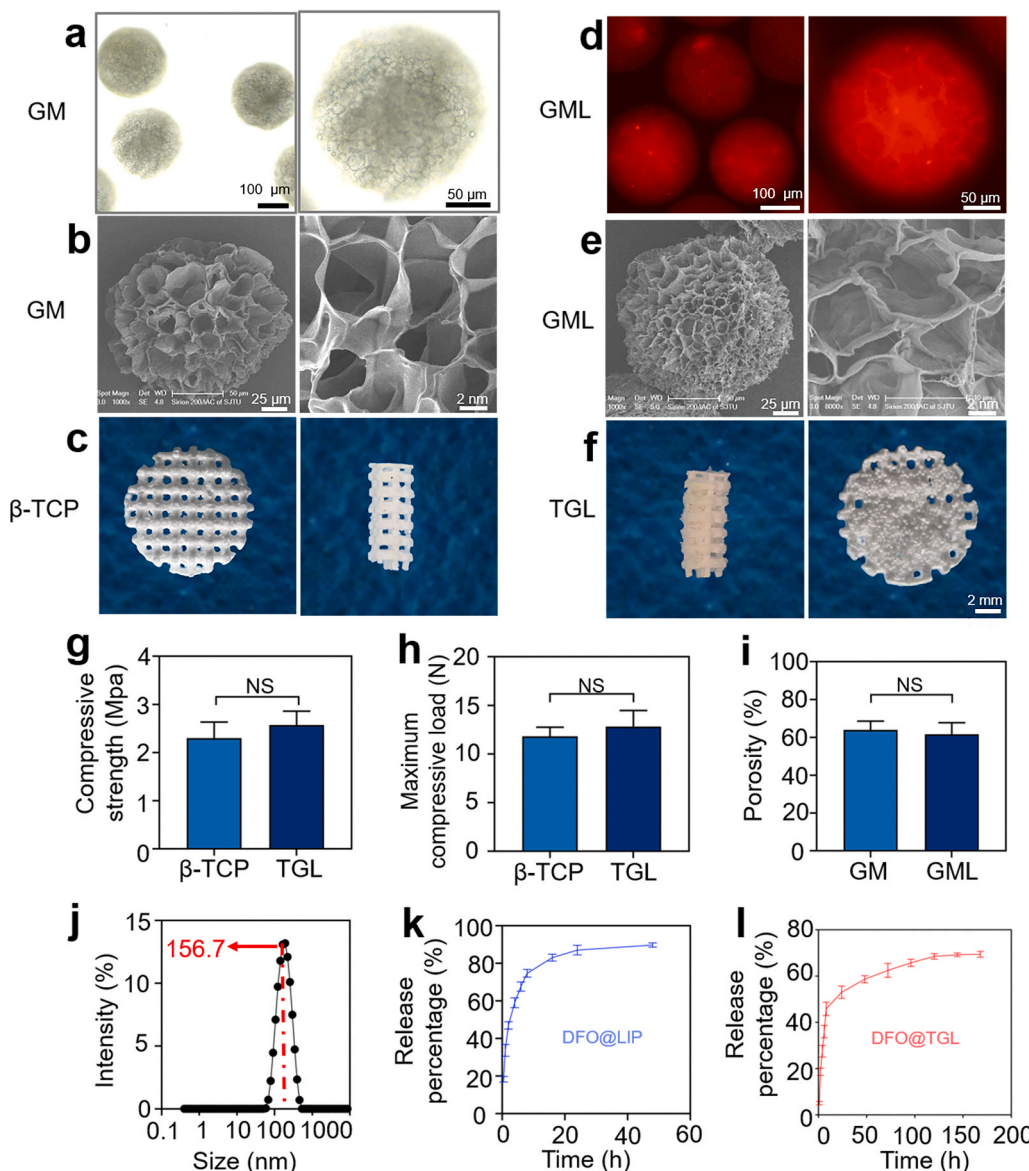


**Fig. 1. Characterization of the scaffolds. (a)** Light microscopic photos of GelMA microspheres (GM). **(b)** SEM images of GelMA Microspheres (GM). **(c)** Digital camera photos of $Ca_3(PO_4)_2$ scaffold (β-TCP). **(d)** Fluorescent microscope images of GelMA Microsphere @ Liposome (GML). **(e)** SEM images of Liposome @ GelMA Microspheres (GML). **(f)** Digital camera photos of GML @ β-TCP (TGL). **(g–h)** Mechanical properties of β-TCP and TGL scaffold. **(I)** Porosity data of GM and GML **(j)** Characterization of liposome particles via DLS. **(k)** The *in vitro* release profile of DFO in the liposome.**(i)** The *in vitro* release profile of DFO in the TGL scaffolds. (T-test, NS, no significant difference.)

deviation. Students-test was applied to compare between two groups, and one-way analysis of variance (ANOVA) was used for statistical tests for comparison between multiple groups. The difference was considered to be statistically significant when P < 0.05.

## 3. .Results

### 3.1. Preparation and characterization of TGL scaffolds

In the present study, GelMA hydrogel microspheres were prepared by microfluidic technology. The diameter of the microspheres was 200 ± 30 μm while the porosity was 64 ± 5%. It could be seen that the prepared microspheres were homogenous in size. The lyophilized microspheres were porous, which was essential for the physical adsorption of drug-loaded liposomes (Fig. 1a and b). Subsequently, an aqueous solution of DFO-loaded liposomes were prepared by reverse evaporation, separated the unencapsulated drugs by ultrafiltration and centrifugation, and tested the encapsulation efficiency by HPLC. The data revealed that the encapsulation rate was 61.5 ± 3%. Simultaneously, DLS was used to detect the particle size distribution of the liposomes. Fig. 1j showed that the liposome particle size was 156.7 ± 4.5 nm, and there is only a single peak indicating dispersion, demonstrating that the uniformity is good. Besides, the polydispersity indexes (PDI) detected by DLS was 0.19 ± 0.03, illustrating the homogeneity of the liposome particles. Next, 3D printing technology was used to prepare porous bioceramics. The application of three-dimensional printing technology in scaffold manufacturing can not only accurately customize the macroscopic geometric size of the scaffold, but also optimize the microscopic porous structure thus promoting bone repair and neovascularization. The ceramic scaffolds prepared in this study were of two specifications: diameter 10 mm, high 2 mm, and diameter 2.5 mm, high 6 mm (Fig. 1c). The micropore diameter of the bioceramic scaffold is 452 ± 51 μm, with the porosity is being 60 ± 8%. The adequate micropore diameter and porosity can not only simulate the three-dimensional porous structure of bone trabeculae but also facilitate the assembly of composite scaffolds [24]. The compressive strength of our porous bioceramic scaffold was 2.2 ± 0.2 MPa right in the range of cancellous bone which was reported being 2–12 MPa, confirming that the bioceramic scaffold can be used for non-load bearing applications of tissue regeneration (Fig. 1g and h) [29]. Fig. 1d shows the liposome @ GelMA microsphere drug delivery system assembled by the immersion adsorption method illustrated by that the GelMA microspheres are excited to a uniform red light under a fluorescence microscope. This is because the fluorescent grafted DFO in the liposomes and the GelMA microspheres were evenly filled with DFO liposomes, which also proved the successful construction of our drug delivery system (Fig. 1d). Besides, the composite scaffold morphology was observed by SEM after freeze-drying. The data showed that the adsorption of liposomes did not change the porosity of GelMA microspheres which is favorable for drug delivery *in vitro* and *in vivo* (Fig. 1e,i). A digital camera was used to take photos once the composite scaffolds were successfully constructed, and the pictures revealed that the pores of the scaffolds were evenly filled with GML, confirming the effective assembling of GML and the porous bioceramic scaffold (Fig. 1f). Compared with the simple biological porous ceramic scaffold, the composite scaffold does not show any increase of mechanical strength, which may be due to the low mechanical support provided by GML (Fig. 1g and h). Fig. 1k was the *in vitro* release profile of DFO @ Lip. Shown from the data, the sudden release effect was obvious in the first 6 h that the cumulative release rate reaching 67.6 ± 2.6%, while the sustained release time *in vitro* was only 48 h. It could be seen that the scaffold loaded with DFO had a rapid release in the first 6 h, with the release rate being about 36% (Figure 1l), which was much lower than the pure DFO loading liposomes and was conducive to the rapid formation of an effective vascular network inside the scaffold in the early stage (Figure 1l). It is the main regulator of vascular growth, which can effectively control angiogenesis and osteogenesis during bone

development and bone repair after injury [30]. In the following 7 days, the release rate reached 69 ± 1.3%, which, on the other hand, had positive significance for the synergistic effects of internal vascularization and osteogenic differentiation in the late repairing process [31,32].

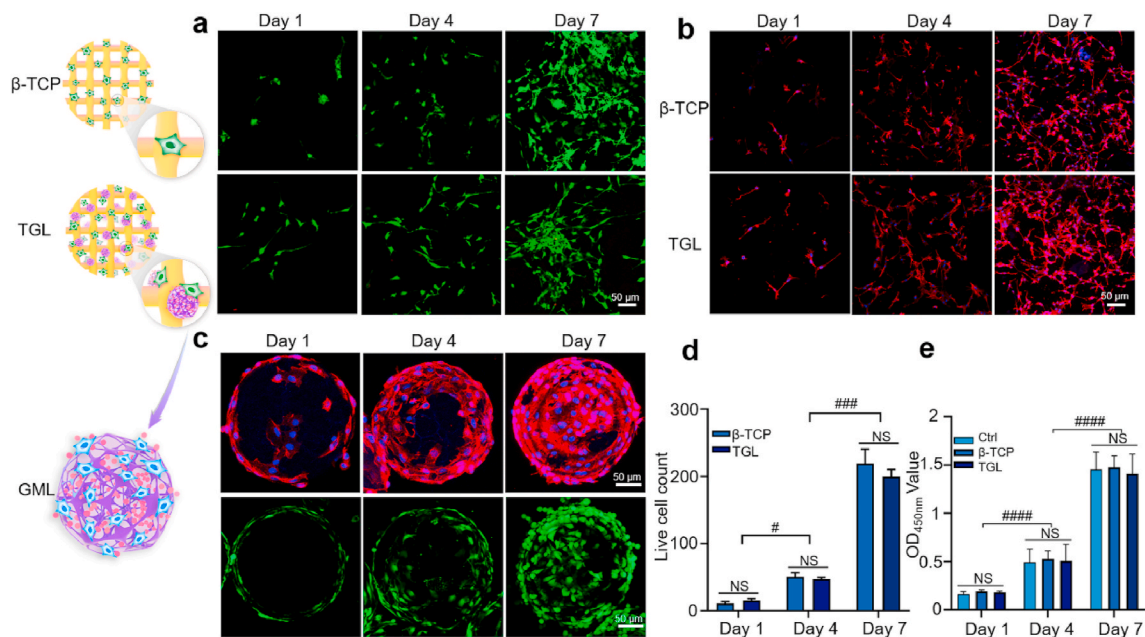### 3.2. In vitro biocompatibility of composite scaffolds

Biocompatibility tests were conducted to investigate the impact of the scaffolds on cytotoxicity and proliferation behavior. Firstly, MC3T3-E1 cells were planted on the surface of a simple scaffold and a composite scaffold, respectively. Seen from Live/Dead staining results, most of the cultured cells on the surface of the scaffolds were alive while few dead cells were observed after 1, 4, and 7 days of culture illustrating good biocompatibility of the composite scaffolds (Fig. 2a–d). Also, cell adherence and extension behavior were further investigated through cytoskeleton staining at 1, 4, and 7 days after co-culturing the cells with various scaffolds. The results revealed that cells displayed a well-stretch morphology and favorable growth and proliferation status on the surface of the scaffolds (Fig. 2b).

In addition, CCK-8 results further revealed that the cellular proliferation activity between two groups after 1, 4, and 7 days culturing (Fig. 2e). Fig. 2c is the result of our observation of GelMA microspheres on the composite scaffold with a laser confocal microscope at given time internals (1, 4, and 7 days). Along with Live/Dead staining, the cytoskeleton staining further confirmed the viability and proliferative abilities of MC3T3-E1 cells. The results altogether demonstrated that both the single ceramic scaffold and a composite scaffold have good biocompatibilities needed for cell survival and consequently for tissue repairing *in vivo*.

### 3.3. In vitro tube formation assessment

Since that bone is rich in blood vessels, the regeneration performance of the scaffolds depends on its ability to induce vascularization at transplant site. Therefore, the effect of β-TCP/TGL on the vascularization process of HUVECs was investigated through a tube-formation assay *in vitro*. Fig. 3a showed that HUVECs cultured in leaching solution of TGL samples displayed much more vascular tube formation compared with that β-TCP and control groups at given time points. More specifically, after 3 h of cell culture, there was no tube formation in the β-TCP and control groups, while a few tubes were formed in the TGL group. Six hours later, larger tubules were observed in the TGL group forming a sharp contrast with β-TCP and control groups illustrating the excellent angiogenesis activity of DFO released from the composite scaffold. Image J was used to calculate total length of formed tubes, number of formed-meshes and junctions, as well as total area per high-power field. The results showed that all calculated parameters in the TGL group were much higher than that in β-TCP and control group, and they all tend to increase over time (Fig. 3b–e). DFO had been reported that it could promote angiogenesis in a dose-dependent manner, and the efficacy of angiogenesis was significantly reduced with a high DFO dose. Hopefully, our results displayed that the TGL scaffolds could release adequate amount of DFO to guide the cellular organization and locomotive activity of HUVECs and showed enhanced tubules generation ability. Studies have found that DFO can induce the expression of Hif1-α and its downstream molecule VEGF and thus promoting blood vessel formation *in vivo* and *in vitro*.

Given that, the Hif1-α signaling pathway was subsequently verified through Western blot and real-time PCR (RT-PCR) studies. After culturing for 24 h, the expression levels of Hif1-α and VEGF in the TGL group were much higher than those in the β-TCP group (Fig. 3f–h), indicating the above conclusions. The RT-PCR results are given in Fig. 3f further confirmed that inducive effect of DFO incorporated into the scaffold. In short, our composite scaffold TGL can effectively release DFO to activate the Hif1-α pathway, thereby up-regulating the expression of VEGF and promoting the rapid formation of blood vessels inside

**Fig. 2.** *In vitro* biocompatibility of 3T3-E1 cells with the scaffolds. **(a)** Live/Dead analysis of 3T3 -E1 cells cultured on the scaffolds on day 1, 4, and 7. Live cells were stained green, while dead cells appeared red. **(b)** The laser scanning confocal microscopic images of MC3T3-E1 cells adhered to the scaffolds for 1, 4 and 7 days. The cytoskeleton was stained in red and the nucleus was blue. **(c)** The survival and proliferation behavior of cells on GML for 1, 4, and 7 days. **(d)** Statistics of the number of living cells. **(e)** CCK-8 assay was used to detect the toxicity of scaffolds. (All the above pictures were taken by confocal microscope. Two-way ANOVA was used; NS, no significant difference; #, P < 0.05; ###, P < 0.001; ####, P < 0.0001). (For interpretation of the references to colour in this figure legend, the reader is referred to the Web version of this article.)
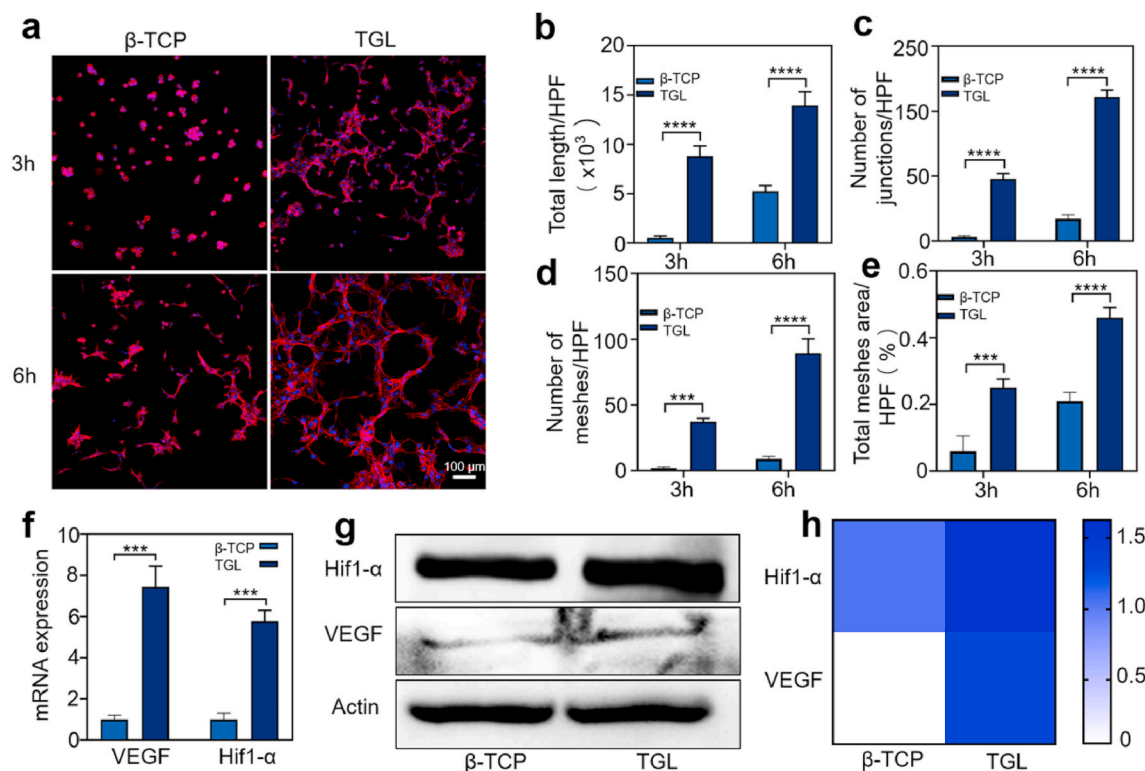


**Fig. 3.** The vascularization studies of β - TCP and TGL scaffolds *in vitro*. **(a)** Endothelial network formation of HUVECs at 3 and 6 h after cell culture. **(b–e)** The differences of total length (b), number of junctions (c), number of meshes (d) and total meshes area per high power field (HPF) were analyzed. (All the above pictures were taken by laser scanning confocal microscope. Two-way ANOVA was used; ***, p < 0.001; ****, p < 0.0001) **(f)** The expression of Hif1-α and VEGF on β-TCP and TGL scaffolds (T-test, ***, p < 0.001). **(g)** The results of Western blot showed that HUVECs were cultured on the scaffold for 24 h. **(h)** Summarized data showing the difference of Hif1-α and VEGF expression of western-blot results.
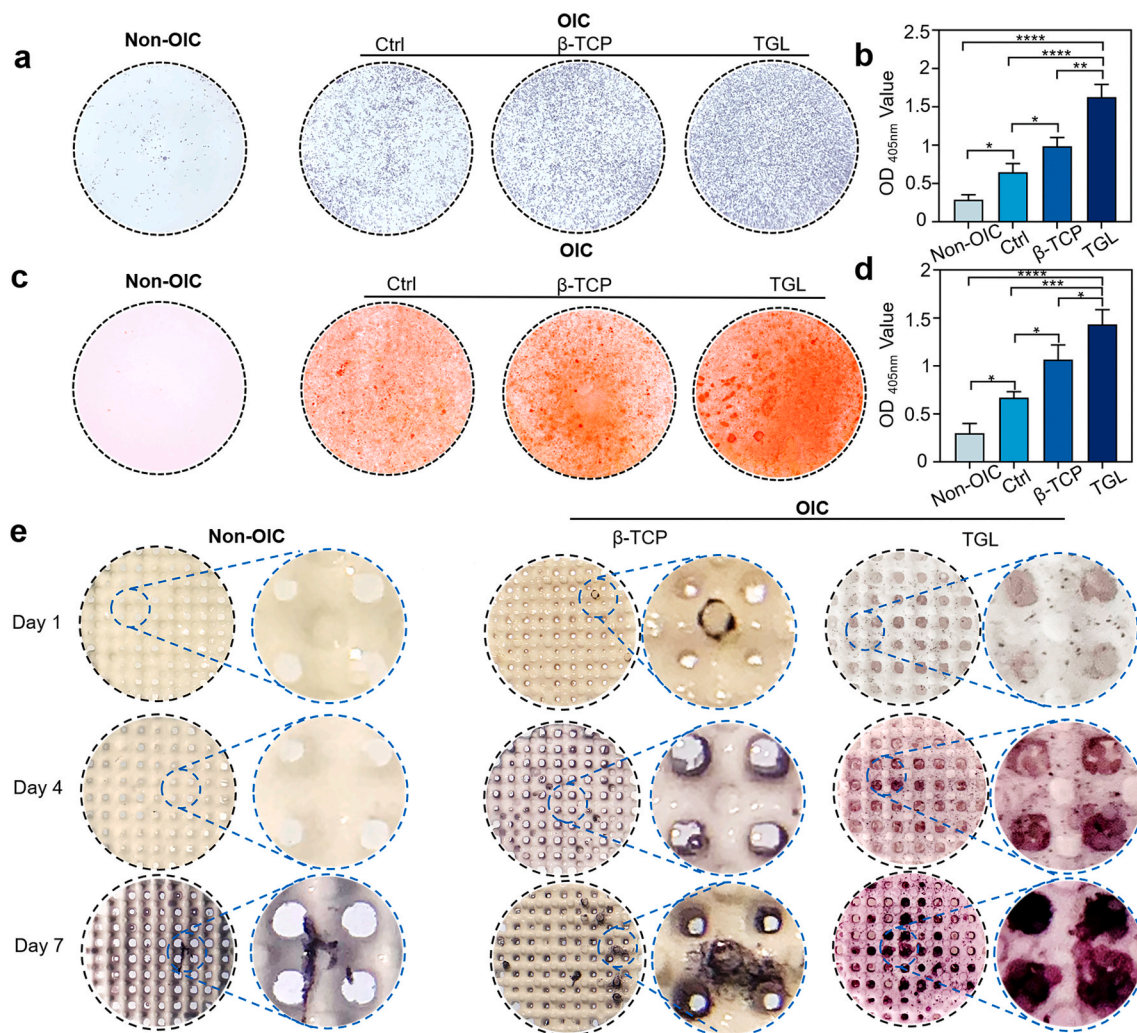
the scaffold.

## 3.4. In vitro osteogenic differentiative inductivity of TGL scaffold on BMSCs

The efficiency of the TGL composite scaffolds to promote the osteogenesis of BMSCs was studied *in vitro*. As osteoblast differentiation is the prerequisite for leading bone regeneration and alkaline phosphatase (ALP) is a marker enzyme of early mature osteoblasts, ALP staining was conducted on day 7 after culturing the BMSCs on the scaffolds (Fig. 4a, Fig. S2). As for the control group, in which cells were cultured in standard medium (Non-OIC), BMSCs did not present any ALP activity at all time points. However, when cultured in the OIC-conditioned medium, the ALP activity of BMSCs was shown in a dark blue on the 7th day, making a striking contrast with the control group. Quantitative analysis showed that on day 7, the TGL group had higher alkaline phosphatase activity (Fig. 4b). Besides, ALP staining experiments were also investigated directly on the surface of the scaffolds at preset time points (1, 4, and 7 days). Fig. 4e illustrated that on the first day, all groups did not show ALP activity, which may be due to the short induction time. On the 4th day, however, the TGL group has the best induction effect as it could

be seen from the local magnification that the pores of the scaffolds were filled with hydrogel microspheres responsible for the excellent induction effects. Predictably, on the 7th day of induction, the ALP activity in the TGL group was the best, and this was in consistence with our previous conclusions and hypothesis. It is generally accepted that in the differentiation process of osteoblasts, the most fundamental biological characteristics are bone matrix synthesis, secretion, and maturation with mineralized nodules being the hallmark of osteoblast differentiation and maturation. Being recognized as an important morphological manifestation of osteogenic function, Alizarin Red S staining was also carried out to verify the mineralization capabilities of rat BMSCs *in vitro*. The results showed that after 14 days of induction, BMSCs in the Non-OIC group did not produce any mineralized nodules, and it was used as a negative control. By contraries, the formation of mineralized nodules could be observed in the OIC group with more intuitive microscopic performance (Fig. 4c). The quantification results further confirmed that TGL could promote the osteogenic activity of BMSCs (Fig. 4d).

To elucidate the effect of TGL on the expression of genes and proteins related to osteogenic differentiation, several target genes and proteins were explored that are crucial in the process of osteogenesis. Because of the time-dependent expression during osteogenesis, the osteogenic



**Fig. 4. Mineralized extracellular matrix production and alkaline phosphatase (ALP) activity of BMSCs were conducted *in vitro*. (a)** Digital photos of rat BMSCs induced by leaching solution of different scaffolds to express alkaline phosphatase activity. **(b)** Uniform statistics were performed at absorbance by quantifying alkaline phosphatase protein expression was quantified through testing the OD value at 405 nm. **(c)** Digital photos of Alizarin red S staining of BMSCs on different scaffolds **(d)** The quantification of Alizarin Red S staining of different groups. **(e)** Results of induction effect of BMSCs of alkaline phosphatase staining on different groups. (Two-way ANOVA was used; NS, no significant difference; *, $p < 0.05$; **, $p < 0.01$; ***, $p < 0.001$; ****; $p < 0.0001$). (For interpretation of the references to colour in this figure legend, the reader is referred to the Web version of this article.)

effect of our composite scaffold on different genes and proteins was tested at 7 and 14 days, respectively. The results of immunofluorescence showed that after seven days of culture in OIC medium, ALP, Runx2, and Osterix in the TGL group were significantly up-regulated than that in β-TCP group, which was used as a negative control group (Fig. 5a–c). The obtained results were in the right consistency with following osteogenic differentiation-related protein detection outcomes, including OSX and type 1collagen (COL 1) (Fig. 6a–d). On the 14th day of coculture, OCN and OPN genes and proteins were also detected on with the results confirming that the osteogenic effect of the TGL composite scaffold was better than that of β - TCP and negative control groups (Fig. 5d and e,6e-h).

It is universally acknowledged that the formation of the bone vascular network is essential for the acquisition of highly functional regenerated tissue. *In vitro*, composite scaffold TGL up-regulated Hif1-α and VEGF proteins by releasing effective DFO, the two key factors in bone vascularization. Besides, VEGF may have a particular function represented by the facts that it not only induces the formation of new blood vessels but also directly affects osteoblasts through the production of BMP by endothelial cells, thus improves the ability of the composite scaffold to induce bone formation. When co-cultured with composite TGL scaffolds, the BMSCs presented a strong mineralized matrix-forming capability and alkaline phosphatase activity. It was further determined with the up-regulated expression of genes and proteins related to osteogenic differentiation induced by the TGL scaffolds. Altogether, the composite 3D printed scaffold effectively combined with DFO possess the osteogenesis functionality as well as the angiogenesis activity *in vitro*.

### 3.5. In vivo bone regeneration assessment of TGL scaffold

With the *in vitro* study results given, the vascularization and osteogenic function of 3D printed TGL scaffold were further studied in rat femoral defect model *in vivo*. The implanted cylindrical scaffolds were in right consistency with the annular defect of the femur during the operation. Throughout the experiment, the rats lived well without any infection or death. At week 2 and 4 after the surgery, the animals were sacrificed and the scaffold explants were obtained for X-ray analysis. The results showed that, in the control group, there was almost no new bone growth during the healing process. For the scaffold groups, new

regenerated bone could be observed over the healing time with the TGL group being the best at each time point (Fig. S4). The consecutive micro-CT images revealed that the dynamic and more precise bone repair process. Through two-dimensional (Fig. 7a) and three-dimensional (Fig. 7b and c) images obtained from Micro-CT together with the micro-architectural parameters, the morphological and quantitative defects of new bone formation were quantitatively analyzed (Fig. 7d).

As for the control group, there was almost no new bone growth during the entire *in vivo* study indicating the successful establishment of critical size bone defect. On the contrary, in the scaffold groups, as the repair process progress, new bone ingrowth can be observed, and the TGL group had the best imaging performance at each time point. Due to the existence of β - TCP, the osteogenesis effect of β-TCP group was also higher than blank control group (Fig. 7a). As time went, much more bone growth was observed at week 4 than 2 weeks. The new osseointegration of the β-TCP group was slightly better than that of the control group, while significantly lower than TGL group at both time points. Three-dimensional reconstruction of the formation of new bone in the defect was then performed, new bone regeneration started from the surrounding edge and moved to the defect center, while there was still a significant drilling defect in the control group throughout the study process. There are several regular channels between the newly formed bone tissue, which indicates that the 3D printed porous scaffold had a supportive role for the growing tissue through its interconnected channels (Fig. 7b and c). The microstructure parameters are also shown in Fig. 7d, the BMD, BV/TV, and Tb·Th of the control group were much lower than those of the scaffold group at both time points. The Tb.Sp was the opposite. It revealed that new bone integration in the TGL group is faster and better than the other groups.

### 3.6. In vivo new blood vessel formation and histological assessment

Histological results of the explants at week 2 and 4 were obtained. HE stained sections displayed the new bones, fibrous tissues, and β-TCP and TGL scaffolds (Fig. 8a). Confirmed from given sections at different time points, there was no evident inflammation or necrosis in each group after implantation. It could be found that the grid-lie scaffolds fulfilled the defect perfectly, and the space between the scaffolds was tucked with newly regenerated mineralized bone along the surface of the pillar. By contrast, the defect area in the control group was not filled, and only
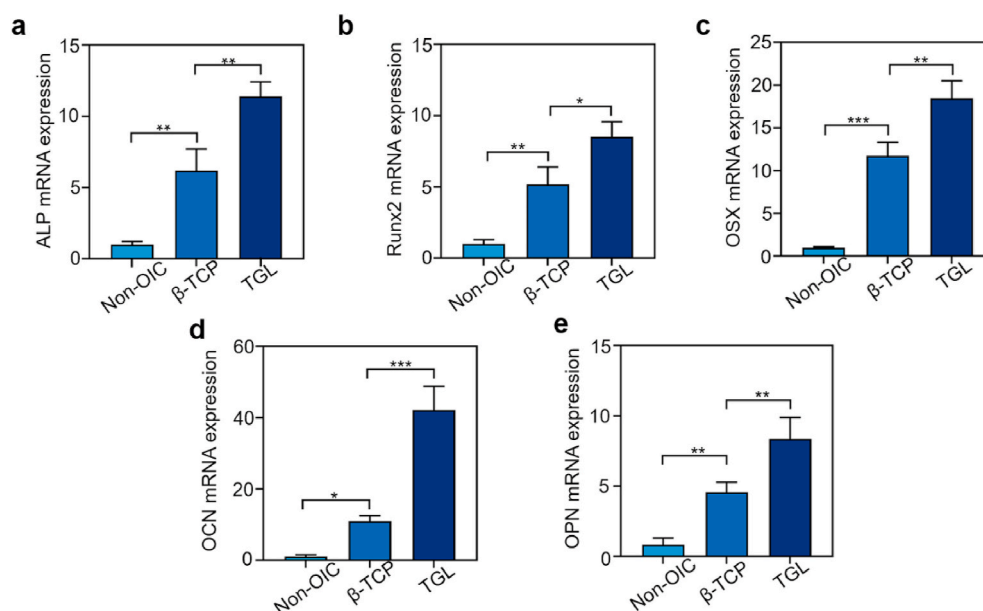
**Fig. 5. Objective to study the effect of scaffolds on the expression of osteogenic genes in rat BMSCs. (a–e)** These genes include Alkaline phosphate (ALP), Runt related transcription factor 2 (Runx2), Osterix (OSX), Osteocalcin (OCN), Osteopontin (OPN) (One-way ANOVA was used; *, $p < 0.05$; **, $p < 0.01$; ***, $p < 0.001$).
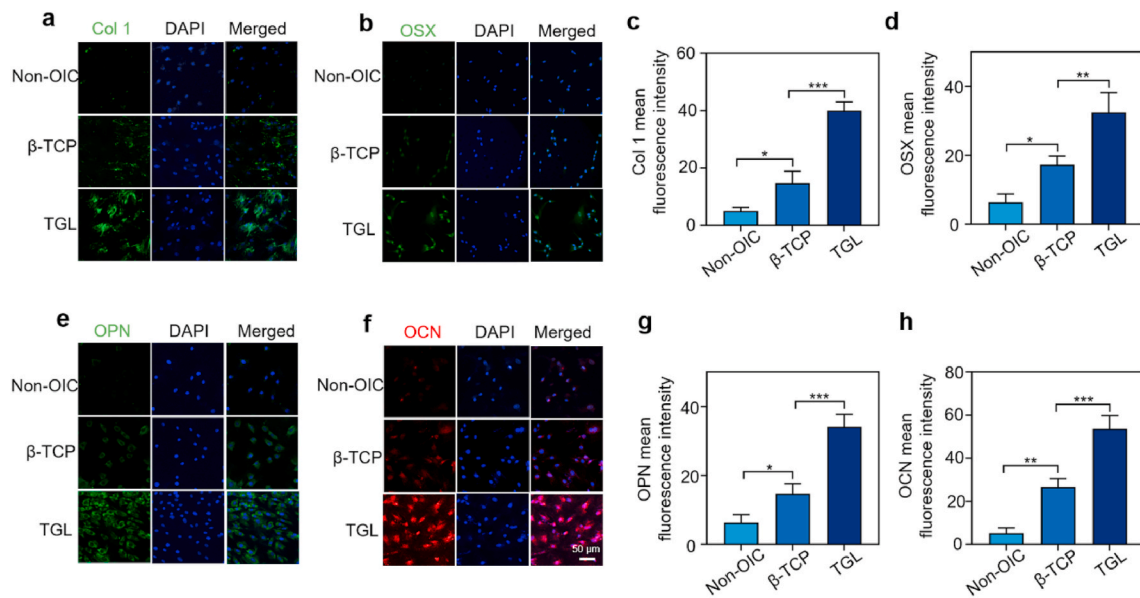
**Fig. 6. Effects of scaffolds on the expression of osteogenic proteins in rat BMSCs. (a, b,e, f)** The effects of scaffolds on the expression of osterix (green), col1 (green), OPN (green) and OCN (red) at 7 and 14 days. The nucleus was counterstained with DAPI (blue). **(c, d, g, h)** Quantification of immunofluorescence intensity. (Two-way ANOVA was used; *, $p < 0.05$; **, $p < 0.01$; ***, $p < 0.001$). (For interpretation of the references to colour in this figure legend, the reader is referred to the Web version of this article.)
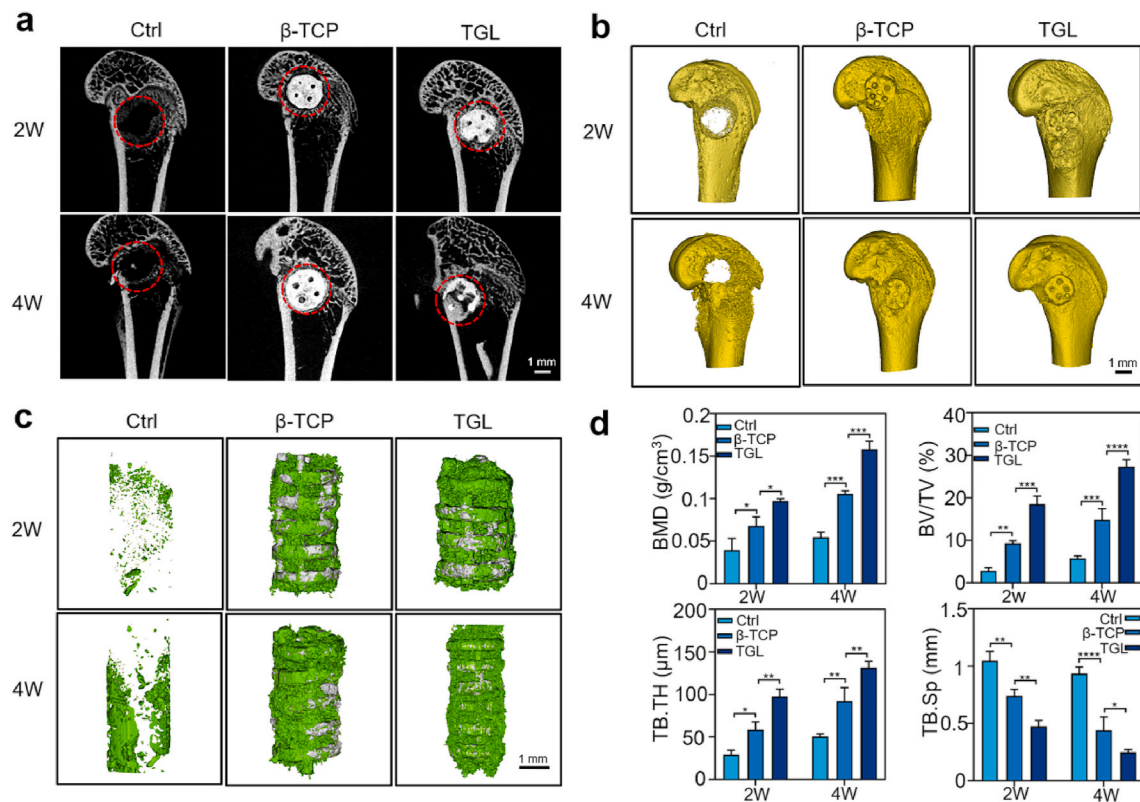


**Fig. 7. Micro CT analysis of osteogenesis *in vivo*. (a)** Micro-CT images of bone defect. The red circle is the site of bone defect constructed by an electric drill. **(b–c)** Three-dimensional reconstruction of Micro-CT images of explanted femurs and the scaffolds respectively showing the regenerative effects of composite scaffolds *in vivo*. **(d)** The three-dimensional reconstructed micro-CT images of different groups were analyzed by image analysis software, 2 and 4 weeks after the scaffold implantation. Microstructural parameters of newly formed bone tissue were summarized, including bone mineral density (BMD), bone tissue volume/total tissue volume (BV/TV), trabecular thickness (Tb·Th) as well as trabecular separation/spacing (Tb.Sp) (One-way ANOVA was used; *, $p < 0.05$; **, $p < 0.01$; ***, $p < 0.001$; ****, $p < 0.0001$). (For interpretation of the references to colour in this figure legend, the reader is referred to the Web version of this article.)
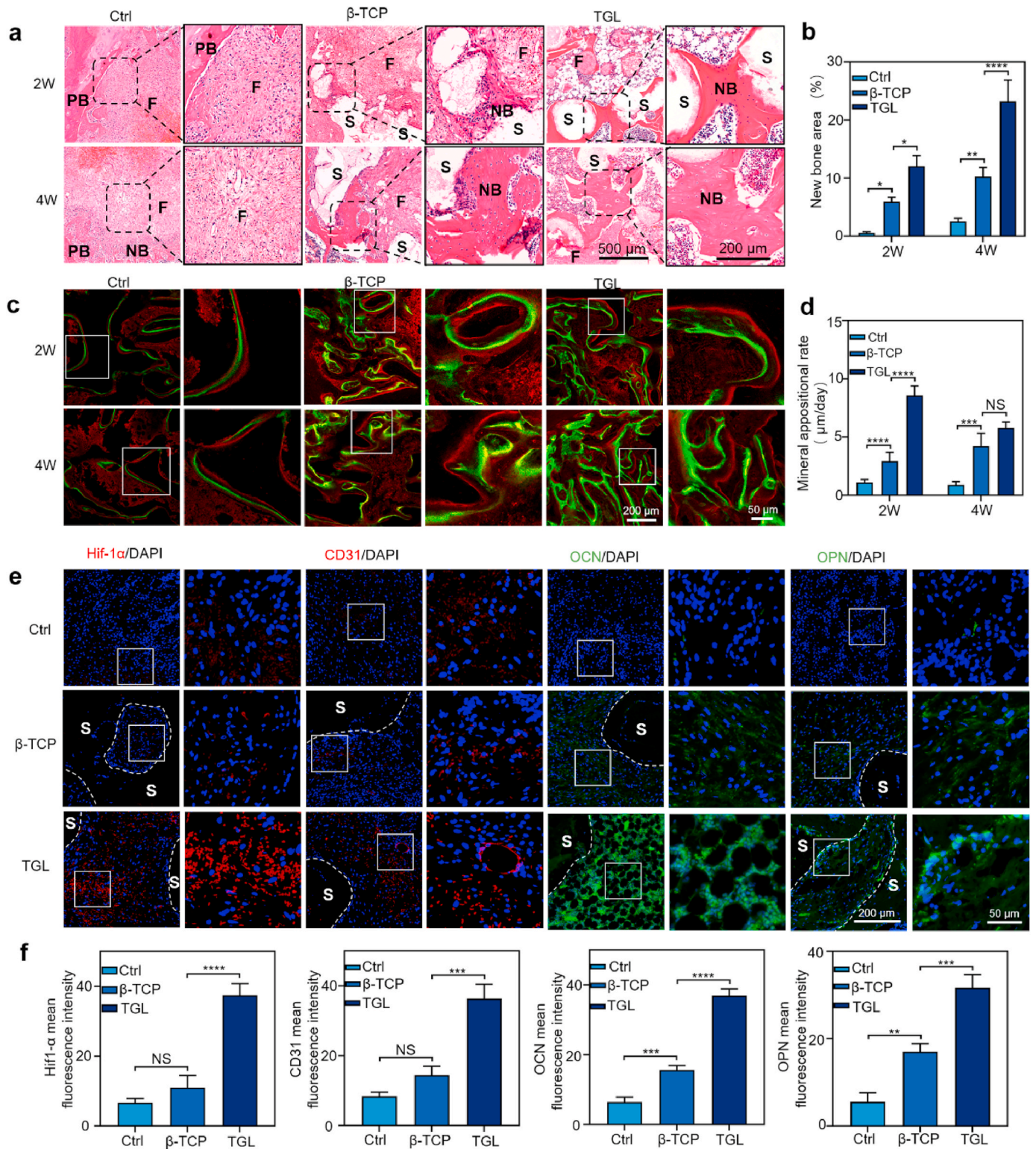
**Fig. 8. Histological analysis of the new regenerated tissues in the defect area with the scaffold implantation. (a)** Representative HE staining images indicating newly formed tissues including newly mineralized bone tissue (NB), fibrous tissue (F) primitive bone (PB) and scaffolds (S). **(b)** The quantification of new bone area in HE staining calculated by Image J software. **(c)** The LSCM scanning results of double calcein labelling at given time points (2 weeks and 4 weeks). The labeled calcein (green) and Alizarin Red S (red) were displayed. The panel in the left is enlarged to clearly show the double marker line. **(d)** The quantitative distance results of two marker lines was summarized. **(e)** Immunofluorescence staining of the decalcified bone slices, the angiogenesis and osteogenesis related genes Hif1-α, CD31, OPN and OCN significantly increased in the TGL group. **(f)** The expression difference of related proteins was quantified. (One-way ANOVA was used; *, $p < 0.05$; **, $p < 0.01$; ***, $p < 0.001$; ****, $p < 0.0001$); NS, no significant difference). (For interpretation of the references to colour in this figure legend, the reader is referred to the Web version of this article.)

a small amount of scattered fibrous tissue was presented. This was indicative that without the support of a scaffold, new bone tissue formation was hardly achieved in a critical sized bone defect. The channels were filled with newly regenerated tissues, indicating that the appropriate pore size and interconnected porous structure in the scaffold were ideal for bone regeneration. The ability of new bone regeneration of all scaffold groups increased with the implantation time went on. β-TCP, being a unique bioceramic scaffold, also promoted osteogenesis compared with the blank control group. As for the TGL group, because of the presence of DFO, the newly formed bone tissues filled every corner of the scaffold, including the center and the edges, observed not only at the surrounding but also in the center area of the implanted scaffolds, which was also indicative of sustained release of DFO, consequently promote the vascularization inside the scaffold, and finally shortened the bone repair time (Fig. 8b).

Furthermore, the above conclusion was further confirmed by the double fluorescence labeling, which displayed a more significant amount of dynamic bone regeneration in the TGL group compared with β-TCP and control ones. It was worth noting that the osteogenesis was more active in two weeks which was quantified by mineral apposition rates (MAR), tending to be stable at week 4, which also perfectly explains that the osteogenic efficiency of the TGL group was much higher than that of the other two groups at week 2. However, there is no significant difference between the TGL and β -TCP groups (Fig. 8c and d).

According to reported studies, DFO can promote the high expression of CD31 in endothelial cells in aged animals consequently promote long bone neovascularization and osteogenesis [33]. To verify whether the Hif1-α pathway was activated during the bone regeneration process after the scaffolds implanted, immunohistochemical tests were performed on the sections of each group at week 4 (Fig. 8e). The results showed that the immunofluorescence was much higher in the TGL group, and it was mainly distributed in the osteoblasts near the new bone. This indicated that the local release of DFO could regulate the expression of Hif1-α and further mediate the specific biological activities. Correspondingly, CD31 immunofluorescence was also strongly expressed in bone endothelial cells which were from newly formed blood vessels.

What's more, the expression levels of OCN and OPN, the osteoblast markers, were also significantly increased in the TGL group. Accordingly, the biological mechanism of angiogenetic and osteogenic function of the TGL scaffold was revealed. We can also draw corresponding conclusions from the subsequent quantitative analysis (Fig. 8f).

## 4. .Discussion

In our previous studies, the coordinated development of mineralized bone and nutrient vessels are two critical factors for the critical size bone defect repair [34]. Without adequate vascular network establishment, the cells at the transplantation site rely on diffusion to deliver nutrients and remove metabolic by-products. However, its effectiveness is limited because of a relatively short transporting distance, usually within a few hundred micrometers [35]. For recent decades, diffusion limitation of bone tissue engineering strategies has always been a significant challenge for its clinical transformation making it necessary that the establishment of a stable and perfuseable vascular network to improve its regeneration potential [36]. DFO can significantly increase bone volume and vascular density at the fracture site in a mouse fracture model [37]. Unfortunately, Drager, J. and colleagues found that directly injection of DFO solution needed to be conducted every 48 h to keep effective drug concentration because the half-life of DFO is only 5–6 h *in vivo* [38]. Therefore, the rapid drug excretion along with with-3D printing structural characteristics, its application in large-scale bone defects had been limited over the decades. Various 3D printed scaffolds are currently being used for bone regeneration; however, poor internal angiogenesis and low osteo-induction ability have always been an unsolved problem. Especially when it comes to large segmental bone defects, the oxygen

and nutrient exchange is limited due to insufficient vascularization, making cell distribution and migration uneven, resulting in newly regenerated bone tissue grows margin-to-center direction. Besides, inspired by the unique biological structure of the "lotus seedpod", these problems were skillfully solved by constructing a 3D printed scaffold with internal blood vessel regeneration ability to stimulate the bone.

The underlying biological mechanisms associated with the observed osseous activities by inducing the Hif1-α pathway via coupling DFO onto scaffolds were also studied. In recent years, with the intensive studies related to Hif1-α in the cellular hypoxia-sensing pathway Thus, it provides a new idea to construct biomaterials for bone repair which is easy to vascularize in the early stage of the bone repair process [39,40]. Hif1-α is continually expressed in cells inhibiting the oxygen-dependent enzymatic activity of prolyl-hydroxylase (PHD) protein under hypoxia [41]. Hif1-α expression initiate the transcription of various hypoxia-related genes, including vascularization, cell survival, cell migration, and proliferation. As for bone, the regulatory role of cellular hypoxia/Hif1-α pathway in the process of bone regeneration, relevant researches data confirmed the relationship between Hif1-α expression and bone remodeling [42]. Once the Hif1-α expression reaches a certain level, it would couple angiogenesis and osteogenesis by regulating the type H vessels resulting in recruitment and activity osteoprogenitor cells [34]. Hif1-α is a strong modulator in tissue engineering, which plays an important role by promoting the osteogenic differentiation of BMSCs [43]. Former studies found that DFO could also indirectly promote osteogenesis by inhibiting the differentiation of osteoclasts, which may be achieved independent of Hif1-α. Except for the recruitment of endothelial progenitor cells, related studies demonstrated that Hif1-α signaling pathway could also be activated by a class of small molecules called hypoxia mimics under normal oxygen conditions. Among them, deferoxamine (DFO) is the most widely studied [30]. It chelates $Fe^{2+}$ required by PHD activity, and iron chelate can activate Hif-1 α/VEGF pathway, thus promoting angiogenesis. Besides, DFO is also the first-line medication used to treat metal iron overload in clinical practice [44]. Focusing on bone regeneration and, studies have reported that DFO can induce cells to express Hif1-α and its downstream molecule VEGF. VEGF is an important intervention factor for blood vessel growth, and it is also deeply involved in the bone regeneration process such as new bone formation and angiogenesis through stimulating vascular invasion and the recruitment of chondrocytes into hypertrophic cartilage [45]. Besides, VEGF can also be released by osteoblasts under hypoxia, inducing endothelial cell migration, proliferation, and vascular permeability [46–48]. On the contrary, BMP-2 can also be produced by endothelial cells to induce osteogenesis. Also, the formation of new tissue during fracture healing depends on successful vascularization [35,36]. Therefore, in this study, DFO as the active ingredient was chose to improve the vascularization and osteogenic properties of the scaffold. However, the high cytotoxicity, off-target disability, and short half-life of DFO severely hindered its further applications. To solve the above problems mainly caused by the sudden release of DFO in 3D printed scaffolds, a drug-carrying system was constructed, namely a liposome @ hydrogel system with stable physical and chemical properties, as well as controllable drug release properties [21]. This drug delivery system not only sustained the ability of DFO to chelate $Fe^{2+}$ but also solved the problem of the controlled release of DFO. In the mid-1960s, when Bangham used transmission electron microscopy to study the behavior of lipids after being immersed in water, the collected lipid-water mixture images showed that the lipids formed water-filled vesicles in the water similar to cells [49]. One substance is named liposome. The self-assembled vesicle structure of liposome can encapsulate not only water-soluble drugs but also transport fat-soluble drugs [50–52]. Marquez et al. prepared liposomes loaded with epidermal growth factor (EGF) and used them to promote the bone repair process [53]. Zhu et al. studied its anti-biofilm activity *in vitro* by constructing a gentamicin sulfate liposome- 3D printed composite scaffold, and the results showed that the composite scaffold showed significant anti-biofilm activity,

which may be an effective strategy for anti-osteomyelitis [54]. However, the low loading efficacy of a single liposome on the scaffold leading to a lower drug loading rate, limiting it is *in vivo* regeneration effects. In recent years, due to its advantages of good biocompatibility, degradability, low cost, and availability, GelMA has been used in a variety of areas of tissue engineering and regenerative medicine [55,56]. Microfluidic technology was used to make GelMA hydrogel microspheres with uniform size and appropriate diameter. The lyophilized microspheres presented a porous structure, which is favorable for the adsorption and release of drugs [16]. Secondly, the constructed GelMA microspheres were preferable for cell adhesion and can be directly incorporated into our 3D printed scaffold without chemical modification, while maintaining the stability and activity of loaded drugs. In this study, a liposome @ hydrogel drug-carrying system was assembled by dipping and adsorbing method. DFO effectively released 35% in the first 6 h and about 69% in the following 7 days. This kind of controlled release is conducive to the rapid growth of blood vessels inside the scaffold in the early stage, while the subsequent maturation of the vascular network and differentiation of BMSCs need to rely on the sustained release of DFO. As we all know, there are two key steps in the bone repair process: intramembranous ossification and endochondral ossification. Mineralized biomaterials promote osteogenesis through the way of intramembranous ossification, which can induce BMSCs to differentiate into osteoblasts both *in vivo* and *in vitro* [34]. Amongst, β-TCP has been believed to have the highest osteo-inductive ability with excellent differentiative effects on BMSCs [57]. Also, compared with the autologous transplantation strategy, the implantation of β-TCP could avoid the formation of fibrous tissue. Therefore, β-TCP was chosen as the raw material for a 3D printed scaffold with appropriate size and porosity. Numerous studies have shown that the appropriate porosity can not only affect the mechanical strength of the scaffold but also can effectively promote the growth of the blood vessels into the scaffold [24]. We proved that the 3D printed composite TGL scaffold could effectively promote the internal vascularization of the scaffold, as well as osteogenic differentiation. Our research results support the powerful potential of internal vascularized 3D printed scaffolds in the bone regeneration field.

## 5. Conclusion

In this study, a 3D printed porous bioceramic scaffold with a bionic "lotus seedpod" structure was successfully constructed that can grow blood vessels inside. The controlled release of DFO enables the scaffold to have an excellent internal vascularization ability in the early stage. It can continuously stimulate the maturation of the internal vascular network of the scaffold and the osteogenic differentiation of BMSCs. The subsequent reconstruction and repair of bone tissue are of great significance. The composite scaffolds exhibited good biocompatibility, internal vascularization abilities, and bone formation potentials *in vitro* experiments. It is further demonstrated that the composite scaffold can promote the growth of blood vessels inside the bone defect in rats and increase the mineralization rate inside the defect, which is crucial to bone regeneration. We believe that this composite scaffold based on the unique biological structure of the "lotus seedpod" will provide a new concept for clinical bone defect repair.

## Declaration of competing interest

The authors declare that the research was conducted in the absence of any commercial or financial relationships that could be construed as a potential conflict of interest.

## Acknowledgments

## Appendix A. Supplementary data

Supplementary data to this article can be found online at https://doi.org/10.1016/j.bioactmat.2020.11.019.

## References

[1] D. Andreev, M. Liu, D. Weidner, K. Kachler, M. Faas, A. Grüneboom, U. Schlötzer-Schrehardt, L. Muñoz, U. Steffen, B. Grötsch, B. Killy, G. Krönke, A. Luebke, A. Niemeier, F. Wehrhan, R. Lang, G. Schett, A. Bozec, Osteocyte necrosis triggers osteoclast-mediated bone loss through macrophage-inducible C-type lectin, J.Clin. Investig 130 (9) (2020) 4811–4830.

[2] R. Prisby, Bone Marrow Microvasculature, Compr.Physiol 10 (3) (2020) 1009–1046.

[3] J. Huang, D. Lin, Z. Wei, Q. Li, J. Zheng, Q. Zheng, L. Cai, X. Li, Y. Yuan, J. Li, Parathyroid hormone derivative with reduced osteoclastic activity promoted bone regeneration via synergistic bone remodeling and angiogenesis, Small 16 (6) (2020), e1905876.

[4] Z. Tang, N. Kong, J. Ouyang, C. Feng, N.Y. Kim, X. Ji, C. Wang, O.C. Farokhzad, H. Zhang, W. Tao, Phosphorus Science-Oriented Design and Synthesis of Multifunctional Nanomaterials for Biomedical Applications, Matter 2 (2) (2020) 297–322.

[5] N. Golafshan, E. Vorndran, S. Zaharievski, H. Brommer, F. Kadumudi, A. Dolatshahi-Pirouz, U. Gbureck, R. van Weeren, M. Castilho, J. Malda, Tough magnesium phosphate-based 3D-printed implants induce bone regeneration in an equine defect model, Biomaterials 261 (2020), 120302.

[6] L. Galea, D. Alexeev, M. Bohner, N. Doebelin, A. Studart, C. Aneziris, T. Graule, Textured and hierarchically structured calcium phosphate ceramic blocks through hydrothermal treatment, Biomaterials 67 (2015) 93–103.

[7] B. Rai, J. Lin, Z. Lim, R. Guldberg, D. Hutmacher, S. Cool, Differences between in vitro viability and differentiation and in vivo bone-forming efficacy of human mesenchymal stem cells cultured on PCL-TCP scaffolds, Biomaterials 31 (31) (2010) 7960–7970.

[8] F. Freeman, P. Pitacco, L. van Dommelen, J. Nulty, D. Browe, J. Shin, E. Alsberg, D. Kelly, 3D bioprinting spatiotemporally defined patterns of growth factors to tightly control tissue regeneration, Sci.Adv 6 (33) (2020), eabb5093.

[9] S. Pan, J. Yin, L. Yu, C. Zhang, Y. Zhu, Y. Gao, Y. Chen, 2D MXene-integrated 3D-printing scaffolds for augmented osteosarcoma phototherapy and accelerated tissue reconstruction, Adv. Sci. 7 (2) (2020), 1901511.

[10] M. Sorkin, A. Huber, C. Hwang, W. Carson, R. Menon, J. Li, K. Vasquez, C. Pagani, N. Patel, S. Li, N. Visser, Y. Niknafs, S. Loder, M. Scola, D. Nycz, K. Gallagher, L. McCauley, J. Xu, A. James, S. Agarwal, S. Kunkel, Y. Mishina, B. Levi, Regulation of heterotopic ossification by monocytes in a mouse model of aberrant wound healing, Nat. Commun. 11 (1) (2020) 722.

[11] P. Lienemann, Q. Vallmajo-Martin, P. Papageorgiou, U. Blache, S. Metzger, A. Kivelió, V. Milleret, A. Sala, S. Hoehnel, A. Roch, R. Reuten, M. Koch, O. Naveiras, F. Weber, W. Weber, M. Lutolf, M. Ehrbar, Smart hydrogels for the augmentation of bone regeneration by endogenous mesenchymal progenitor cell recruitment, Adv. Sci. 7 (7) (2020), 1903395.

[12] L. Veschini, D. Belloni, C. Foglieni, M. Cangi, M. Ferrarini, F. Caligaris-Cappio, E. Ferrero, Hypoxia-inducible transcription factor-1 alpha determines sensitivity of endothelial cells to the proteosome inhibitor bortezomib, Blood 109 (6) (2007) 2565–2570.

[13] W. Cheng, Z. Ding, X. Zheng, Q. Lu, X. Kong, X. Zhou, G. Lu, D. Kaplan, Injectable hydrogel systems with multiple biophysical and biochemical cues for bone regeneration, Biomaterials Sci 8 (9) (2020) 2537–2548.

[14] Y. Xue, J. Yang, J. Luo, J. Ren, Y. Shen, D. Dong, Y. Fang, L. Hu, M. Liu, Z. Liao, J. Li, Z. Fang, P. Shang, Disorder of iron metabolism inhibits the recovery of unloading-induced bone loss in hypomagnetic field, J. Bone Miner. Res. 35 (6) (2020) 1163–1173.

[15] A. Donneys, Q. Yang, M. Forrest, N. Nelson, T. Zhang, R. Ettinger, K. Ranganathan, A. Snider, S. Deshpande, M. Cohen, S. Buchman, Implantable hyaluronic acid-deferoxamine conjugate prevents nonunions through stimulation of neovascularization, NPJ Regen.Med 4 (2019) 11.

[16] J. Yang, Y. Han, J. Lin, Y. Zhu, F. Wang, L. Deng, H. Zhang, X. Xu, W. Cui, Ball-Bearing-Inspired Polyampholyte-Modified Microspheres as Bio-Lubricants Attenuate Osteoarthritis, Small, Weinheim an der Bergstrasse, Germany, 2020, e2004519.

[17] J.Y.A. B, Y.Z. B, F.W. A, L.D. A, X.X. B, W.C. A, Microfluidic liposomes-anchored microgels as extended delivery platform for treatment of osteoarthritis, Chem. Eng. J. 400.

[18] L. Liu, Y. Xiang, Z. Wang, X. Yang, W. Cui, Adhesive liposomes loaded onto an injectable, self-healing and antibacterial hydrogel for promoting bone reconstruction, NPG Asia Mater. 11 (1) (2019) 81.

[19] Y. Bi, L. Han, Y. Zheng, Y. Guan, H. Zhang, S. Ge, H. Wang, Q. Jia, Y. Zhang, S. Zhang, Lotus-seedpod-bioinspired 3D superhydrophobic diatomite porous

ceramics comodified by graphene and carbon nanobelts, ACS Appl. Mater. Interfaces 10 (32) (2018) 27416–27423.

[20] F. Wu, M. Zhang, Y. Bai, X. Wang, R. Dong, C. Wu, Lotus seedpod-derived hard carbon with hierarchical porous structure as stable Anode for sodium-ion batteries, ACS Appl. Mater. Interfaces 11 (13) (2019) 12554–12561.

[21] C. Ruoyu, Y. Yufei, L. Han, C. Hao, P. Guoqing, D. Lianfu, C. Wenguo, Mechanically enhanced lipo-hydrogel with controlled release of multi-type drugs for bone regeneration, Appl.Mater.Today 12 (2018) 294–308.

[22] M. Zhang, R. Lin, X. Wang, J. Xue, C. Deng, C. Feng, H. Zhuang, J. Ma, C. Qin, L. Wan, J. Chang, C. Wu, 3D printing of Haversian bone-mimicking scaffolds for multicellular delivery in bone regeneration, Sci.adv. 6 (12) (2020) eaaz6725.

[23] D. Lee, C. Cha, Cell subtype-dependent formation of breast tumor spheroids and their variable responses to chemotherapeutics within microfluidics-generated 3D microgels with tunable mechanics, Mater Sci Eng C Mater Biol Appl 112 (2020), 110932.

[24] K. Burg, S. Porter, J. Kellam, Biomaterial developments for bone tissue engineering, Biomaterials 21 (23) (2000) 2347–2359.

[25] Y. Luo, D. Zhai, Z. Huan, H. Zhu, L. Xia, J. Chang, C. Wu, Three-dimensional printing of hollow-struts-packed bioceramic scaffolds for bone regeneration, ACS Appl. Mater. Interfaces 7 (43) (2015) 24377–24383.

[26] D. Lee, K. Lee, C. Cha, Microfluidics-assisted fabrication of microtissues with tunable physical properties for developing an in vitro multiplex tissue model, Adv. Biosyst. 2 (12) (2018) 12.

[27] H. Kim, C. Song, C. Cha, J. Jung, J. Oh, Refined fabrication of mechano-stimulating micro-platform for on-chip analyses of complex platelet behavior, J. Ind. Eng. Chem. 84 (2020) 269–279.

[28] W. Liu, J. Li, M. Cheng, Q. Wang, K. Yeung, P. Chu, X. Zhang, Zinc-modified sulfonated polyetheretherketone surface with immunomodulatory function for guiding cell fate and bone regeneration, Adv. Sci. 5 (10) (2018), 1800749.

[29] K. Gómez-Lizárraga, C. Flores-Morales, M. Del Prado-Audelo, M. Álvarez-Pérez, M. Piña-Barba, C. Escobedo, Polycaprolactone- and polycaprolactone/ceramic-based 3D-bioplotted porous scaffolds for bone regeneration: a comparative study, MAT SCI ENG C-MATER 79 (2017) 326–335.

[30] Q. Ran, Y. Yu, W. Chen, X. Shen, C. Mu, Z. Yuan, B. Tao, Y. Hu, W. Yang, K. Cai, Deferoxamine loaded titania nanotubes substrates regulate osteogenic and angiogenic differentiation of MSCs via activation of HIF-1α signaling, MAT SCI ENG C-MATER 91 (2018) 44–54.

[31] Q. Yao, Y. Liu, J. Tao, K. Baumgarten, H. Sun, Hypoxia-Mimicking nanofibrous scaffolds promote endogenous bone regeneration, ACS Appl. Mater. Interfaces 8 (47) (2016) 32450–32459.

[32] C. Guo, K. Yang, Y. Yan, D. Yan, Y. Cheng, X. Yan, N. Qian, Q. Zhou, B. Chen, M. Jiang, H. Zhou, C. Li, F. Wang, J. Qi, X. Xu, L. Deng, Sf-deferoxamine, A bone-seeking angiogenic drug, prevents bone loss in estrogen-deficient mice, Bone 120 (2019) 156–165.

[33] M. Yang, C. Li, X. Sun, Q. Guo, Y. Xiao, T. Su, M. Tu, H. Peng, Q. Lu, Q. Liu, H. He, T. Jiang, M. Lei, M. Wan, X. Cao, X. Luo, MiR-497~195 cluster regulates angiogenesis during coupling with osteogenesis by maintaining endothelial Notch and HIF-1α activity, Nat. Commun. 8 (2017) 16003.

[34] A. Kusumbe, S. Ramasamy, R. Adams, Coupling of angiogenesis and osteogenesis by a specific vessel subtype in bone, Nature 507 (7492) (2014) 323–328.

[35] K. Sivaraj, R. Adams, Blood vessel formation and function in bone, Dev. (Cambridge, England) 143 (15) (2016) 2706–2715.

[36] P. Chandra, A. Atala, Engineering blood vessels and vascularized tissues: technology trends and potential clinical applications, Clin.Sci (London, England 133 (9) (1979) 1115–1135, 2019.

[37] E. Quinlan, S. Partap, M. Azevedo, G. Jell, M. Stevens, F. O'Brien, Hypoxia-mimicking bioactive glass/collagen glycosaminoglycan composite scaffolds to enhance angiogenesis and bone repair, Biomaterials 52 (2015) 358–366.

[38] J. Drager, J. Ramirez-GarciaLuna, A. Kumar, U. Gbureck, E. Harvey, J. Barralet, Hypoxia biomimicry to enhance monetite bone defect repair, Tissue Eng. 23 (2017) 1372–1381.

[39] C. Wan, S. Gilbert, Y. Wang, X. Cao, X. Shen, G. Ramaswamy, K. Jacobsen, Z. Alaql, A. Eberhardt, L. Gerstenfeld, T. Einhorn, L. Deng, T. Clemens, Activation of the hypoxia-inducible factor-1alpha pathway accelerates bone regeneration, Proc. Natl. Acad. Sci. U. S. A. 105 (2) (2008) 686–691.

[40] Y. Wang, C. Wan, L. Deng, X. Liu, X. Cao, S. Gilbert, M. Bouxsein, M. Faugere, R. Guldberg, L. Gerstenfeld, V. Haase, R. Johnson, E. Schipani, T. Clemens, The hypoxia-inducible factor alpha pathway couples angiogenesis to osteogenesis during skeletal development, J. Clin.Investig 117 (6) (2007) 1616–1626.

[41] D. Komatsu, M. Hadjiargyrou, Activation of the transcription factor HIF-1 and its target genes, VEGF, HO-1, iNOS, during fracture repair, Bone 34 (4) (2004) 680–688.

[42] G. Semenza, HIF-1 and mechanisms of hypoxia sensing, Curr. Opin. Cell Biol. 13 (2) (2001) 167–171.

[43] Y. Yan, H. Chen, H. Zhang, C. Guo, K. Yang, K. Chen, R. Cheng, N. Qian, N. Sandler, Y. Zhang, H. Shen, J. Qi, W. Cui, L. Deng, Vascularized 3D Printed Scaffolds for Promoting Bone Regeneration, Biomaterials, 2019, pp. 97–110.

[44] F. Fierro, A. O'Neal, J. Beegle, M. Chávez, T. Peavy, R. Isseroff, J. Egaña, Hypoxic pre-conditioning increases the infiltration of endothelial cells into scaffolds for dermal regeneration pre-seeded with mesenchymal stem cells, Fron Cell Dev Biol 3 (2015) 68.

[45] S. Fang, S. Chen, H. Nurmi, V. Leppänen, M. Jeltsch, D. Scadden, L. Silberstein, H. Mikkola, K. Alitalo, VEGF-C Protects the Integrity of Bone Marrow Perivascular Niche, Blood, 2020.

[46] C. Wang, K. Huang, Y. Sun, Y. Yang, J. Ko, L. Weng, F. Wang, VEGF modulates angiogenesis and osteogenesis in shockwave-promoted fracture healing in rabbits, J. Surg. Res. 171 (1) (2011) 114–119.

[47] J. Dai, A. Rabie, VEGF: an essential mediator of both angiogenesis and endochondral ossification, J. Dent. Res. 86 (10) (2007) 937–950.

[48] I. Eshkar-Oren, S. Viukov, S. Salameh, S. Krief, C. Oh, H. Akiyama, H. Gerber, N. Ferrara, E. Zelzer, The forming limb skeleton serves as a signaling center for limb vasculature patterning via regulation of Vegf, Dev. (Cambridge, England) 136 (8) (2009) 1263–1272.

[49] A.D. Bangham, Liposomes: the babraham connection, Chem. Phys. Lipids 64 (1–3) (1993) 275.

[50] K. Mei, Y. Liao, J. Jiang, M. Chiang, M. Khazaieli, X. Liu, X. Wang, Q. Liu, C. Chang, X. Zhang, J. Li, Y. Ji, B. Melano, D. Telesca, T. Xia, H. Meng, A. Nel, Liposomal delivery of mitoxantrone and a cholesteryl indoximod prodrug provides effective chemo-immunotherapy in multiple solid tumors, ACS Nano 14 (10) (2020) 13343–13366.

[51] A. Singh, A. Biswas, A. Shukla, P. Maiti, Targeted therapy in chronic diseases using nanomaterial-based drug delivery vehicles, Signal Transduct Tar 4 (1) (2019) 33.

[52] A. Gabizon, H. Shmeeda, E. Tahover, G. Kornev, Y. Patil, Y. Amitay, P. Ohana, E. Sapir, S. Zalipsky, Development of Promitil®, a lipidic prodrug of mitomycin c in PEGylated liposomes: from bench to bedside, Adv. Drug Deliv. Rev. S0169-409X (20) (2020) 30111–30113.

[53] L. Marquez, F.A.N.M. De Abreu, C.L. Ferreira, G.D. Alves, M.N. Miziara, J.B. Alves, Enhanced bone healing of rat tooth sockets after administration of epidermal growth factor (EGF) carried by liposome, Injury 44 (4) (2013) 558–564.

[54] C.T. Zhu, Y.Q. Xu, J. Shi, J. Li, J. Ding, Liposome combined porous beta-TCP scaffold: preparation, characterization, and anti-biofilm activity, Drug Deliv. 17 (6) (2010) 391.

[55] H. Hu, L. Dong, Z. Bu, Y. Shen, J. Luo, H. Zhang, S. Zhao, F. Lv, Z. Liu, miR-23a-3p-abundant small extracellular vesicles released from Gelma/nanoclay hydrogel for cartilage regeneration, J Extracell Vescicles 9 (1) (2020), 1778883.

[56] X. Zhang, G. Chen, Y. Liu, L. Sun, L. Sun, Y. Zhao, Black phosphorus-loaded separable microneedles as responsive oxygen delivery carriers for wound healing, ACS Nano 14 (5) (2020) 5901–5908.

[57] T. Yu, Q. Liu, T. Jiang, X. Wang, Y. Yang, Y. Kang, Channeled β-TCP scaffolds promoted vascularization and bone augmentation in mandible of beagle dogs, Adv. Funct. Mater. 26 (37) (2016) 6719–6727.